


Article

An Opto-Electro-Thermal Model for Black-Silicon Assisted Photovoltaic Cells in Thermophotovoltaic Applications

Jasman Y.-H. Chai, Basil T. Wong * and Jaka Sunarso 

Research Centre for Sustainable Technologies, Faculty of Engineering, Computing and Science,
Swinburne University of Technology, Kuching 93350, Malaysia

* Correspondence: twong@swinburne.edu.my

Abstract: Black silicon (b-Si)-assisted photovoltaic cells have textured b-Si surfaces, which have excellent light-trapping properties. There has been a limited amount of work performed on the theoretical modelling of b-Si photovoltaic cells, and hence, in this work, a coupled optical-electrical-thermal model has been proposed for the simulation of b-Si photovoltaic cells. In particular, the thermal aspects in b-Si photovoltaic cells have not been discussed in the literature. In the proposed model, the finite-difference time-domain (FDTD) method was used to study the optical response of the b-Si photovoltaic cell. Semiconductor equations were used for the electrical modelling of the cell. For the thermal model, the Energy Balance Transport Model was used. The developed model was used to simulate b-Si photovoltaic cells under thermophotovoltaic sources. The impacts of heat generation on the electrical performance of thermophotovoltaic cells are discussed. Simulation results from this study showed that black silicon layer improved efficiency and power output in thermophotovoltaic cells compared to thermophotovoltaic cells with no surface texture. In addition, heat generation due to Joule heating and electron thermalization in b-Si-assisted thermophotovoltaic cells reduced the open-circuit voltage and electrical performance.

Keywords: black silicon; numerical simulation; photovoltaics; silicon thermophotovoltaics



Citation: Chai, J.Y.-H.; Wong, B.T.; Sunarso, J. An Opto-Electro-Thermal Model for Black-Silicon Assisted Photovoltaic Cells in Thermophotovoltaic Applications. *Photonics* **2023**, *10*, 565. <https://doi.org/10.3390/photonics10050565>

Received: 28 February 2023

Revised: 10 April 2023

Accepted: 9 May 2023

Published: 11 May 2023



Copyright: © 2023 by the authors. Licensee MDPI, Basel, Switzerland. This article is an open access article distributed under the terms and conditions of the Creative Commons Attribution (CC BY) license (<https://creativecommons.org/licenses/by/4.0/>).

1. Introduction

Surface texturing is an effective way to improve the efficiencies of photovoltaic cells. Black silicon (b-Si) is a type of surface that has been shown to achieve lower reflectance than conventional textured surfaces [1]. A black silicon (b-Si) surface has silicon nanostructures that can assist in light trapping and improve the efficiency of photovoltaic cells or the performance of photoelectric devices. This surface can be produced by various etching methods and has exceptional light-trapping properties, which are especially useful for photovoltaic applications. However, in the literature, there is a lack of a theoretical model that describes the conversion of energies in a b-Si photovoltaic cell. Most studies have focused on only the optical aspects of a b-Si surface, with few, if any, focusing on the coupled opto-electro-thermal modelling of a b-Si photovoltaic cell [2–16]. In several studies, the electrical modelling of the b-Si photovoltaic cells has been brief and often assumed an ideal light-to-electrical-energy conversion, disregarding the effects of recombination and other losses [4,5,10,16]. In this study, a complete opto-electro-thermal simulation model was developed for the theoretical simulation of b-Si photovoltaic cells. The simulation model was used to simulate the efficiency of a b-Si photovoltaic cell in thermophotovoltaic (TPV) applications.

In the literature, most optical and electrical simulations performed for b-Si photovoltaic cells have been de-coupled. For studies performing coupled simulations, assumptions such as zero recombination or losses have led to an overestimation of electrical performances. In one study by Lin and Povinelli [5], for instance, the efficiency of a Si-nanowire-based photovoltaic cell was estimated from the optical absorption in the cell, disregarding recombination effects, which hence may have led to an overestimation of the cell efficiency.

They have used the FDTD and transfer matrix method for their simulations. In a different simulation study by Rahman and Boden [10], a coupled optoelectrical simulation study has been performed using commercial software packages Lumerical FDTD and Sentaurus TCAD, respectively, for the optical and electrical simulations. This is one of the few studies providing insights into a coupled simulation, but the thermal aspects of the b-Si photovoltaic cell have not been studied. In a few other studies, other simulation methods have also been used, including the rigorous coupled wave analysis (RCWA) [3,14] and finite element method (FEM) [7,15], but these methods focus only on the optical properties of a photovoltaic cell. Rigorous electrical simulations, such as using the popular semiconductor equations, have not been conducted for b-Si photovoltaic cells. In addition, thermal modelling in b-Si photovoltaic cells and photovoltaic cells, in general, have been brief and given little focus on [1]. Hence, due to the lack of a holistic simulation model for b-Si photovoltaic cells, this study aims to propose a complete model for bridging the gap.

2. Methodology

In the simulation model, there will be three models describing the exchange of energy in the photovoltaic cells: the (1) optical model, (2) electrical model, and (3) thermal model. An illustration of the simulated device is shown in Figure 1. The energy transfer process described by these models can be seen in Figure 2. In short, in the optical model, the carrier generation rate will be calculated from the incident radiation using the FDTD method. In the electrical model, the semiconductor equations will be used to calculate the electrical responses, including output currents and efficiency, of the cell. In the thermal model, the Energy Balance Transport Model (EBTM) is used to calculate the amount of heat generation and temperature rise in the cell. A flowchart showing the overall simulation flow is shown in Figure 3. In the following sections, the equations used to describe the energy transfer in the three models will be described in detail.

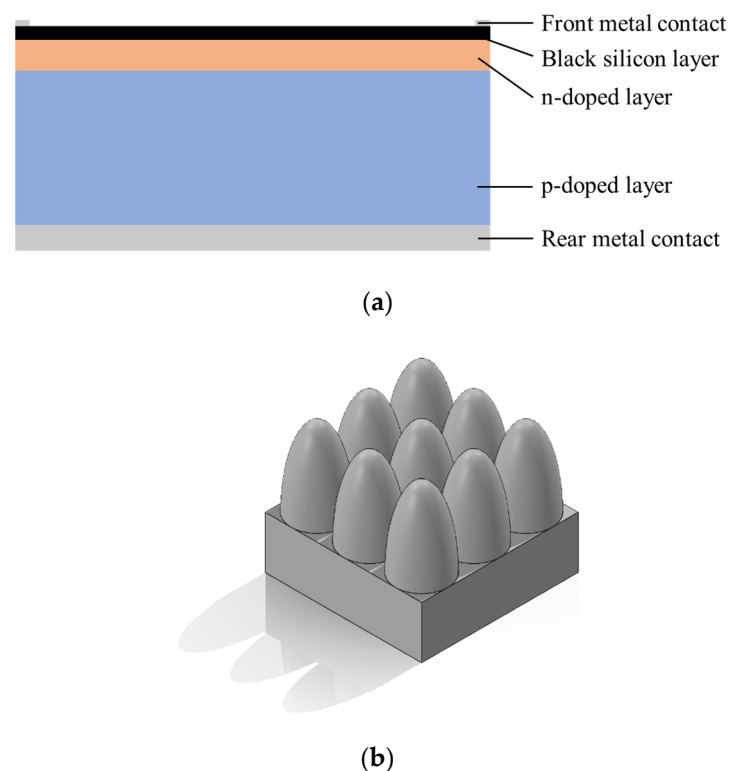


Figure 1. Illustration of (a) a photovoltaic cell with a b-Si layer, (b) a cell consisting of several b-Si nanostructures.

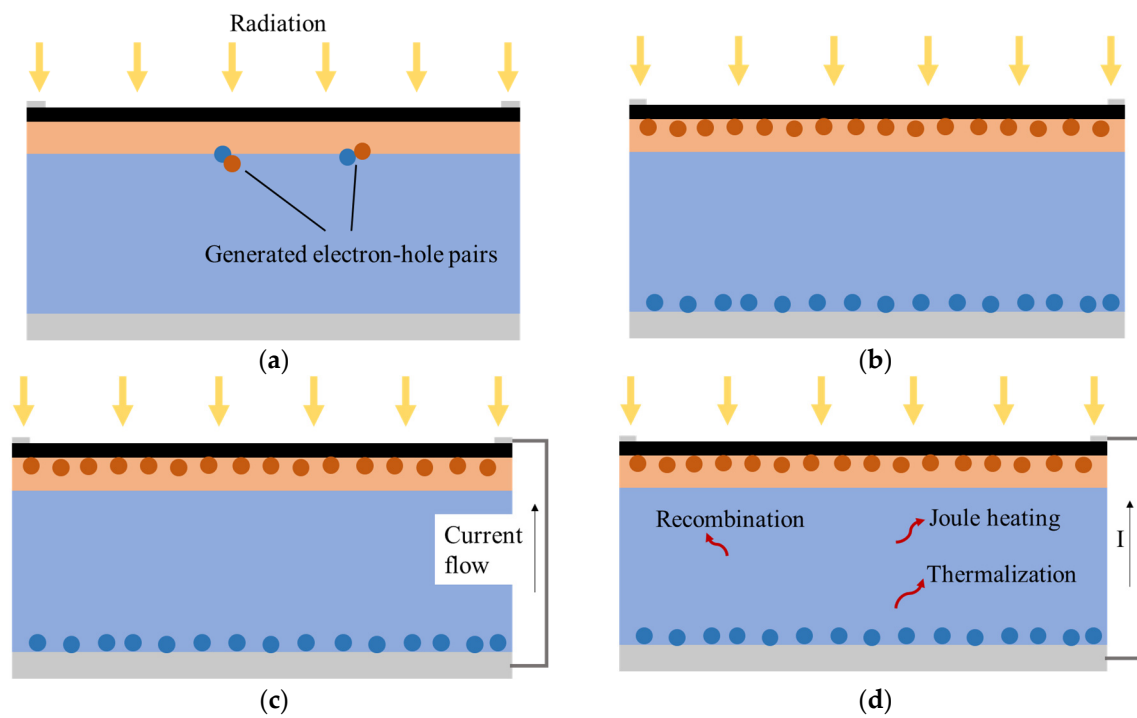


Figure 2. (a) Generation of electron-hole pairs from absorption of radiation, (b) potential accumulation in the p and n regions, (c) current flow due to potential difference, and (d) heat generation mechanisms in an operating cell.

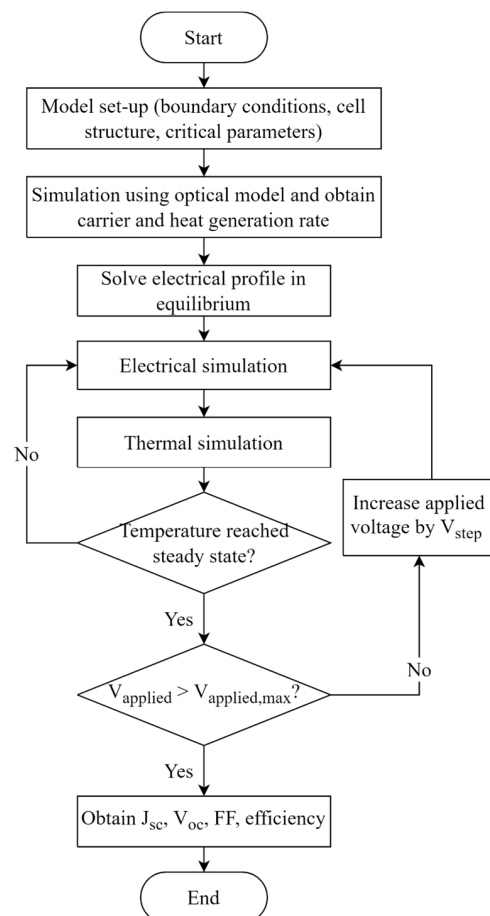


Figure 3. Process flow of the complete simulation model.

2.1. Optical Model

An in-house developed FDTD model [17] was used to simulate the b-Si nanostructures. It was preferred over macroscale models such as ray tracing, as the b-Si nanostructures usually had sizes of less than one micron, and the FDTD method could capture diffraction effects in these periodic structures. In the FDTD method, the update equations for the propagation of electric and magnetic fields (\vec{E} and \vec{H}) in a staggered Yee grid [18] were given by:

$$-\frac{1}{\mu} \vec{\nabla} \times \vec{E} = \frac{\vec{H}\left(t + \frac{\Delta t}{2}\right) - \vec{H}\left(t - \frac{\Delta t}{2}\right)}{\Delta t} \quad (1)$$

$$\frac{1}{\epsilon} \vec{\nabla} \times \vec{H} = \frac{\vec{E}(t + \Delta t) - \vec{E}(t)}{\Delta t} \quad (2)$$

These updated equations describe the propagation of the electromagnetic waves in a simulation domain with specified material regions. A full description of the FDTD method can be found elsewhere [19,20]. Periodic boundary conditions are used in horizontal directions. On the top and bottom boundaries, the perfectly matched layer (PML) boundary condition is used. The complex refractive index of silicon was obtained from the work of Green and Keevers [21]. To obtain the output data, the steady-state field values were obtained by applying a discrete Fourier transform to the time-domain field values. Power flowing through the reflection and transmission planes and the normalised reflectance (R) and transmittance (T) were calculated using Equations (3) and (4):

$$P_{z,R/T}(\lambda, r) = \frac{1}{2} \text{Re} \left(E_{x,R/T}(\lambda, r) H_{y,R/T}^*(\lambda, r) - E_{y,R/T}(\lambda, r) H_{x,R/T}^*(\lambda, r) \right) \cdot A(r) \quad (3)$$

$$R/T(\lambda) = \frac{\sum_r P_{z,R/T}(\lambda, r)}{P_{\text{src}}(\lambda)} \quad (4)$$

where λ is wavelength, r is the positional vector, A is the area of the plane, and P_{src} is the power of the source pulse. The power absorbed can be calculated from the steady-state electric field using Equation (5):

$$P_A(\lambda, r) = -\frac{1}{2} \left| \vec{E}(\lambda, r) \right|^2 \cdot \sigma(\lambda, r) \cdot V_{\text{cell}} \quad (5)$$

and the absorptance can be calculated using Equation (4) of a similar form. Here, σ is the optical conductivity and V_{cell} is the volume of a cell.

The range of dimensions of the simulated b-Si nanostructures is selected based on the analysis from the review of Chai et al. [1] on the typical b-Si dimensions producible using current technologies. Diameters range from 50 to 650 nm, and heights range from 200 to 1800 nm.

2.2. Electrical Model

In this model, the semiconductor equations in Equations (6)–(10) will be used to solve for the current–voltage characteristics in the b-Si photovoltaic cell. They consist of Poisson's equation, continuity equations, and the drift-diffusion current equations. The derivation of these equations can be found in the textbooks by Wuerfel [22] and Entner [23] for further reading. The equations are:

$$\nabla \cdot \nabla V = -\frac{q}{\epsilon} (p - n + N_D - N_A) \quad (6)$$

$$\nabla \cdot \vec{J}_n - q \frac{\partial n}{\partial t} = q (R_{\text{net}} - G_{\text{opt}}) \quad (7)$$

$$\nabla \cdot \vec{J}_p + q \frac{\partial p}{\partial t} = -q(R_{\text{net}} - G_{\text{opt}}) \quad (8)$$

$$\vec{J}_n = qn\mu_n \vec{E} + qD_n \nabla n \quad (9)$$

$$\vec{J}_p = qp\mu_p \vec{E} - qD_p \nabla p \quad (10)$$

where V is the electrostatic potential, q is the elementary charge, ϵ is the permittivity, p and n represent the hole and electron concentration, respectively, $\vec{J}_{n/p}$ is the current density of electrons/holes, R_{net} is the net recombination rate, μ is the carrier mobility, \vec{E} is the electric field, D is the diffusion constant, and N_D and N_A are the concentration of charged impurity donors and acceptors. We also note the following relationships:

$$\vec{E} = -\nabla V \quad (11)$$

$$D_{n,p} = \mu_{n,p} \frac{k_B T}{q} = \mu_{n,p} (v_T)_{n,p} \quad (12)$$

where k_B is the Boltzmann constant, T is the local temperature, and v_T is the thermal voltage. Assuming steady-state condition and substituting Equations (9)–(12) into Equations (6)–(8), we eliminate \vec{E} and $\vec{J}_{n,p}$ and obtain the Poisson and continuity equations in terms of V :

$$\nabla \cdot \nabla V = \frac{q}{\epsilon} (n - p + N_A - N_D) \quad (13)$$

$$-\nabla \cdot (n\mu_n \nabla V) + \nabla \cdot (\mu_n v_{T,n} \nabla n) = R_{\text{net}} - G_{\text{opt}} \quad (14)$$

$$-\nabla \cdot (p\mu_p \nabla V) - \nabla \cdot (\mu_p v_{T,p} \nabla p) = -(R_{\text{net}} - G_{\text{opt}}) \quad (15)$$

To solve these equations, Gummel's scheme and Slotboom's formulation [24] are used. In short, for the Slotboom formulation, the carrier concentrations are replaced by Slotboom variables that are written as follows:

$$n = \Phi_n e^{\bar{V}} \quad (16)$$

$$p = \Phi_p e^{-\bar{V}} \quad (17)$$

$$\Phi_n = n_i e^{-\frac{q\phi_n}{k_B T}} \quad (18)$$

$$\Phi_p = n_i e^{\frac{q\phi_p}{k_B T}} \quad (19)$$

$$\bar{V} = \frac{qV}{k_B T} \quad (20)$$

These Slotboom variables are then substituted into the semiconductor equations, and they are discretised using the finite difference method. After discretisation, the non-linear simultaneous equations are then solved following Gummel's scheme, as described in the work of Vasileska et al. [24]. A summary of Gummel's scheme is shown in the flowchart in Figure 4.

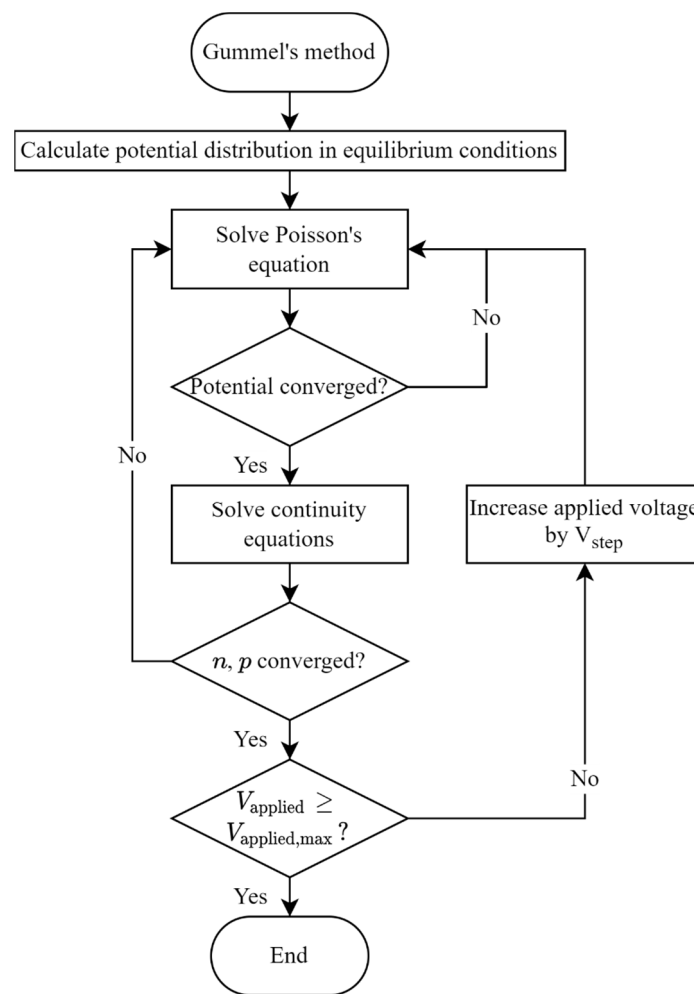


Figure 4. Flowchart showing the iterative flow of Gummel's method.

At the boundaries, Dirichlet boundary conditions are specified for the potentials and carrier concentrations. At the boundaries:

$$V_{\text{boundary}} = V_{\text{eq}} + V_{\text{applied}} \quad (21)$$

$$\text{n-type semiconductor : } n_{\text{boundary}} = \frac{1}{2} \left(\sqrt{N_D^2 + 4n_i^2} + N_D \right); p_{\text{boundary}} = \frac{n_i^2}{n} \quad (22)$$

$$\text{p-type semiconductor : } p_{\text{boundary}} = \frac{1}{2} \left(\sqrt{N_A^2 + 4n_i^2} + N_A \right); n_{\text{boundary}} = \frac{n_i^2}{p} \quad (23)$$

where $V_{\text{eq}} = \frac{k_B T}{q} \ln \frac{N}{n_i}$ is the potential in equilibrium conditions with zero applied bias.

2.3. Thermal Model

In this research, the EBTM, a modification from Stratton's method [25], with an electron–phonon scattering model, is used to simulate the heating effects and temperature distribution in the simulated photovoltaic device. In the EBTM, the temperatures for three different populations—electrons, optical phonons, and acoustic phonons—will need to be calculated. This method has been adapted from the review by Grassler et al. [26] to include the effects of electron thermalization in photovoltaic cells. In short, the three

equations below govern the electron, optical phonon, and acoustic phonon temperatures in the photovoltaic cell:

$$\frac{dS_n}{dx} = J_n \cdot E + H_{\text{therm}} - W_n. \quad (24)$$

$$C_{LO} \frac{\partial T_{LO}}{\partial t} = \frac{3}{2} n k_B \left(\frac{T_e - T_{LO}}{\tau_{e-LO}} \right) - C_{LO} \left(\frac{T_{LO} - T_A}{\tau_{LO-A}} \right) \quad (25)$$

$$C_A \frac{\partial T_A}{\partial t} = \frac{d}{dx} \left(k_L \frac{dT_A}{dx} \right) + H \quad (26)$$

where S_n is the electron energy flux density, H_{therm} is the thermalized electron power, W_n is the energy loss density from the electrons, $T_{e/LO/A}$ is the electron/optical phonon/acoustic phonon temperature, τ are the respective relaxation times, $C_{A/LO}$ is the acoustic/optical phonon heat capacity, and H is a heating term that will be described below. The discussion on the derivation of these equations can be found in other works [25–27]. The energy loss density and heating terms are described by the equations below:

$$W_n = \frac{3}{2} k_B n \left(\frac{T_n - T_{LO}}{\tau_{e-LO}} + \frac{T_n - T_A}{\tau_{e-A}} \right) + E_g (G_{\text{impact}} - R_{\text{Auger}}) \quad (27)$$

$$H = C_{LO} \left(\frac{T_{LO} - T_A}{\tau_{LO-A}} \right) + \frac{3}{2} k_B n \left(\frac{T_n - T_A}{\tau_{e-A}} \right) + E_g R_{\text{SRH}} \quad (28)$$

For Equation (24), the electron energy flux density S_n is dependent on the electron temperature and current flowing through the node, and they are related by the equations:

$$S_n = -k_n \frac{dT_n}{dx} - \frac{k_B \delta_n}{q} J_n T_n \quad (29)$$

$$k_n = q n \mu_n \left(\frac{k_B}{q} \right)^2 \Delta_n T_n. \quad (30)$$

where k_n is the electron thermal conductivity, and δ_n and Δ_n are custom-fitted coefficients that are dependent on the assumptions made on the interactions between the particles in the system [26]. Discretising Equations (24)–(26), the non-linear equations can be solved iteratively to obtain solutions for the electron and phonon temperatures, as shown in the flowchart in Figure 5.

The thermal boundary conditions are convective for both the top and bottom surfaces. These boundary conditions can be written as follows:

$$\left(k \frac{dT}{dx} \right)_{\text{top/bottom}} = h_{\text{top/bottom}} (T_{\text{top/bottom}} - T_{\infty}). \quad (31)$$

However, for the bottom boundary, another equation is used to define the temperature distribution across the metal contact layer. The following equation applies:

$$\left(k \frac{dT}{dx} \right)_{\text{bottom}} = k_{\text{metal}} \frac{T_{\text{interface}} - T_{\text{bottom}}}{t_{\text{metal}}} \quad (32)$$

where $T_{\text{interface}}$ is the temperature at the interface between the semiconductor layer and the metal layer. For the electron energy conservation equation, an insulated boundary is assumed on both surfaces of the semiconductor layer. Hence, the only pathway for loss of energy in electrons is through energy transfer to optical phonons and acoustic phonons. This insulated boundary is written as follows:

$$\left(\frac{dT_n}{dx} \right)_{\text{boundary}} = 0 \quad (33)$$

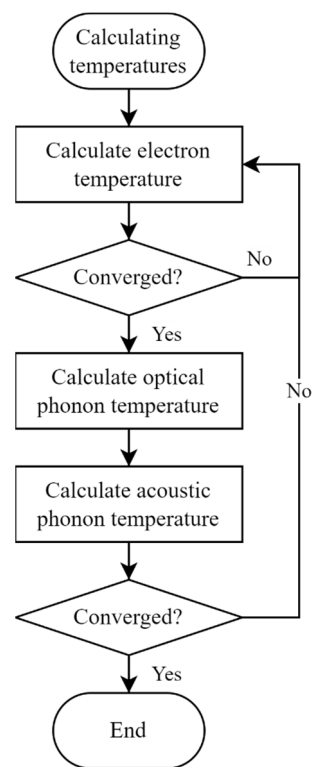


Figure 5. Simulation flow when solving for the temperature distributions for the electrons, optical phonons, and acoustic phonons.

3. Results

3.1. Verification of the Simulation Program

To confirm the accuracy of the developed simulation program, simulation results from commercial and open-source simulation programs have been used as a reference. Each of the simulation models (optical and electrical) is verified to ensure that each model is accurately programmed. For the optical model, the 3D simulation results from the work of Rahman and Boden [10] were used to verify the data. In the article, they simulated a 3D b-Si surface with periodic cylindrical nanostructures using the Lumerical FDTD Solutions. In addition, they have also compared the simulation results with experimental data in their study. The nanostructures had a diameter of 140 nm, height of 360 nm, and pitch of 280 nm in a hexagonal arrangement. Figure 6a shows that the optical model produced outputs similar to the commercial software. However, the slight deviations were attributed to the slight differences in the input permittivity values used.

To verify the simulated performance of a photovoltaic cell obtained using the developed program, a simulated J-V curve of the cell under solar illumination was compared to the results obtained using PC1D. For recombination, SRH recombination, Auger recombination, and impact ionization models were used. For mobility, the Arora model was used for low-field mobility, and the Caughey–Thomas model was used for field-dependent mobility [28]. The comparison of the J-V curves obtained is shown in Figure 6b. It was noted that there were slight differences due to the constants used in the different models. For the J-V curve obtained, the parameters of the simulated photovoltaic device are shown in Table 1.

For the thermal model, the obtained simulation results are compared to results from the work of Zhou et al. [29]. Due to the limitations of the EBTM and limited studies on the heat generation in thin photovoltaic cells, only a 20 μm -thick photovoltaic cell was simulated. For thicker cells, it would require a large number of computational resources, which were, unfortunately, inaccessible in the current study. The simulated temperature rise from this configuration was compared to the one simulated by Zhou et al. [29], and the

dimensions are presented in Table 2. In both simulated cells, the AM1.5G spectrum has been used as the incident spectrum.

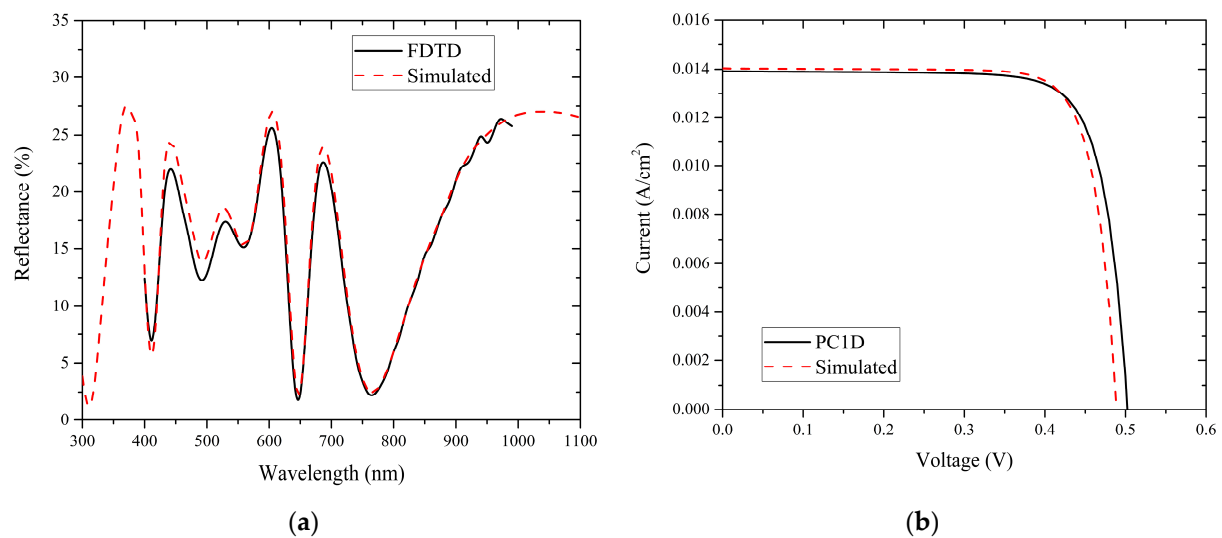


Figure 6. (a) Comparison of optical simulation results with results from Lumerical FDTD Solutions, (b) Comparison of electrical simulation results with results from PC-1D.

Table 1. Cell parameters for the simulated device.

Cell thickness	20 μm
N-doped layer thickness	0.5 μm
Donor concentration	10^{18} cm^{-3}
P-doped layer thickness	19.5 μm
Acceptor concentration	10^{16} cm^{-3}
Cell temperature	300 K

Table 2. Configurations of simulated cells in this study and the study by Zhou et al.

Reference	This study	Zhou et al. [29]
Top glass cover thickness (μm)	N/A	3200
Encapsulant thickness (μm)	N/A	500
Silicon cell thickness (μm)	20	200
Backsheet layer thickness (μm)	N/A	300
Ambient temperature (K)	300	303

The temperature in the cell has been obtained and is shown in Figure 7. It was noted that the lattice temperature was represented by the acoustic phonon temperatures. From the figure, the acoustic phonon temperature had risen about 8.5 K to about 308.5 K, which was lower than the temperature rise obtained in the study of Zhou et al. of about 27 K. The larger temperature rise in the work of Zhou et al. was attributed to the large absorption due to a thick cell thickness, insulation due to the glass and encapsulant layers, and parasitic heat absorption from these layers. To emulate the impacts of having the insulative layers, the convective heat transfer coefficient h at both the top and bottom boundaries was lowered to obtain the temperature rise in the cell. Table 3 lists the temperature rise of the simulated cell at different h values. It was observed that the temperature rise was higher when h decreased (analogous to having an insulation layer). Hence, if the insulative glass and encapsulant layers were absent, the temperature rise in the cell would be lower.

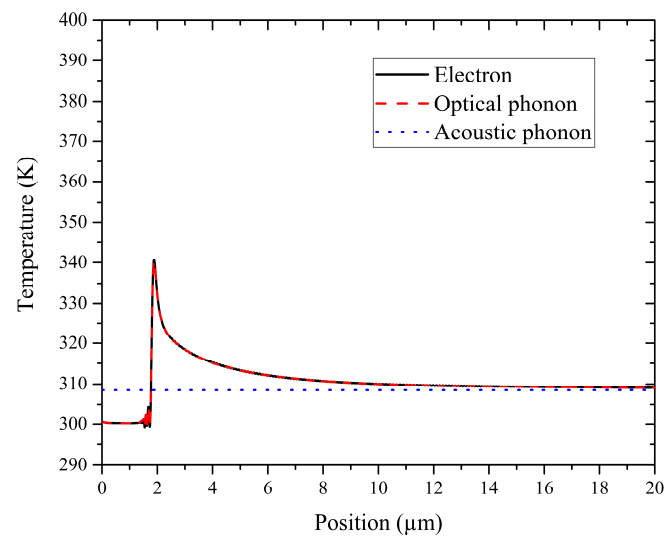


Figure 7. Temperature distribution of different energy carriers.

Table 3. Temperature rise for different h values.

Convective heat transfer coefficient, h (W/m ² -K)	1	0.001
Temperature rise, ΔT (K)	8.5	19.7

While the comparison was not exhaustive, it showed that the temperature rise from the simulation model was within the expected range of values. To confirm the accuracy of the simulated results, a further comparison may be needed, which will be discussed in future work.

3.2. Impact of the b-Si Layer on the Thermophotovoltaic Performance

The developed simulation model was used to simulate the impacts of a b-Si layer on the performance and efficiency of a TPV cell. A simple comparison was given for two TPV cells with and without the b-Si layer. The configuration of the simulated b-Si cell is given in Table 4. The TPV source was the spectrum from a Yb₂O₃ emitter at 1735 K [30,31], which was the typical selective emitter used for silicon TPV applications. The spectrum is shown in Figure 8. Firstly, the optical performances of the TPV cells were compared. Figure 9 shows the reflectance and absorptance spectra for both cases. It was noted that the transmittance was zero as the metal layer had a large permittivity and was opaque in the simulated wavelength range. By comparing these graphs, the reflectance for the flat silicon photovoltaic cell was much higher than the photovoltaic cell with a b-Si surface, especially in the visible light wavelength range. This was because the flat surface caused a sudden jump in the refractive index between the air and the photovoltaic cell, causing a significant amount of reflection, as described by the Fresnel equations for reflection and transmission. On the other hand, the photovoltaic cell with a b-Si surface recorded a much lower reflection in most of the wavelength's range. This was attributed to the refractive index gradient existing in the b-Si layer [1,32]. Due to the refractive index gradient, the incident EM wave did not reflect off easily, improving the absorptance in the cell.

Table 4. Device parameters for the simulated silicon photovoltaic cell.

B-Si nanostructure shape	Paraboloid
B-Si nanostructure height	600 nm
B-Si nanostructure diameter	350 nm
Period of b-Si nanostructure	350 nm
Cell thickness (excluding the b-Si layer)	50 μm
Emitter dopant concentration	10^{17} cm^{-3}
Base dopant concentration	10^{17} cm^{-3}
Rear metal layer thickness	300 nm

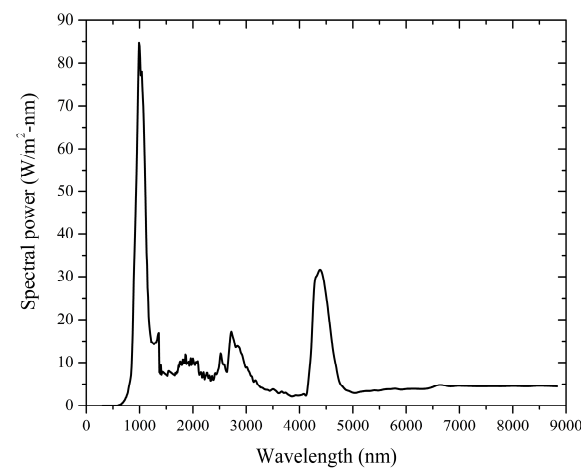


Figure 8. Spectral power emitted by Yb_2O_3 emitter at 1735 K.

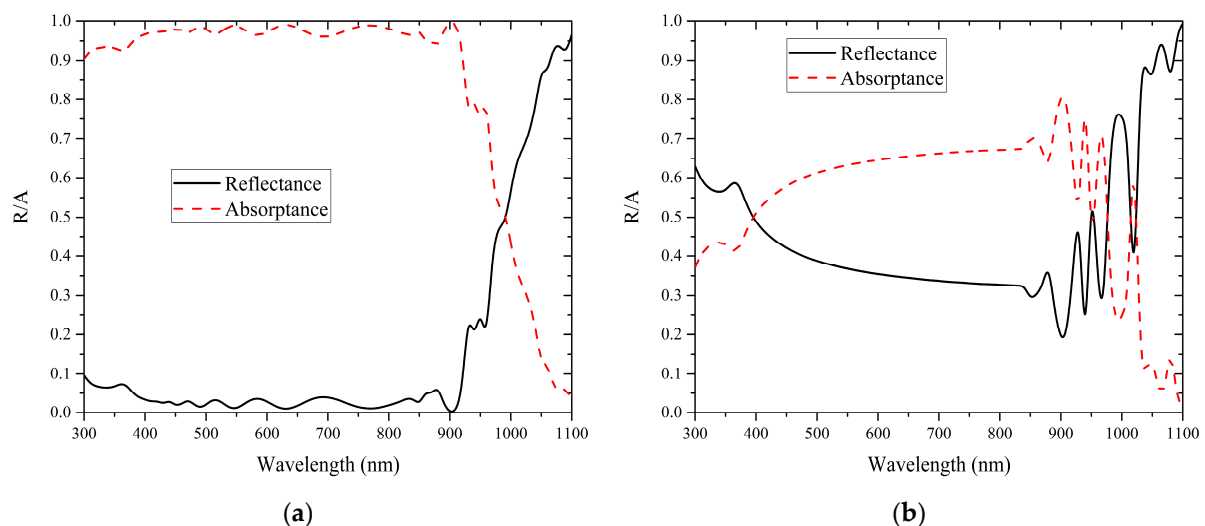


Figure 9. RTA curve for the photovoltaic cell with (a) b-Si surface, (b) flat Si surface.

To compare the electrical performances, the efficiencies of the cells are compared. Similarly, the efficiencies are simulated across different n-doped emitter thicknesses to identify the optimum doping thickness. The efficiency curve with respect to the doping thickness is shown in Figure 10 for both the flat Si and b-Si cells. As expected, the b-Si cell performed better than the flat Si cell across all n-doped emitter thicknesses. It is noted that the efficiency is low compared to solar applications due to the abundance of energies lower than the band gap of silicon in the source spectrum shown above. In addition, the J-V curves of the b-Si and flat-Si cells at 11.6 μm of n-layer thickness are compared in Figure 11.

The short-circuit currents are also noticeably higher in the b-Si cell compared to the flat Si cell, with a similar open circuit voltage. As a result, the maximum power point for the b-Si cell is also higher, by about 30%. These observations have shown the contribution of the b-Si layer on the performance of a TPV cell. It is noted that the short circuit current density values are high compared to the ones obtained in solar applications. In short, the high current density values are due to the differences in the source spectra in both solar applications and TPV applications. In the AM1.5G spectrum, the integrated power is about 1000 W/m^2 , while, for the Yb_2O_3 spectrum used, the integrated power is about 5 times this power. The input power density is much higher for the TPV spectrum and hence would increase the amount of output current and power density. On the other hand, the photons in the Yb_2O_3 spectrum are concentrated in $>800\text{nm}$ wavelength region and are more efficiently absorbed and lose less energy through thermalization.

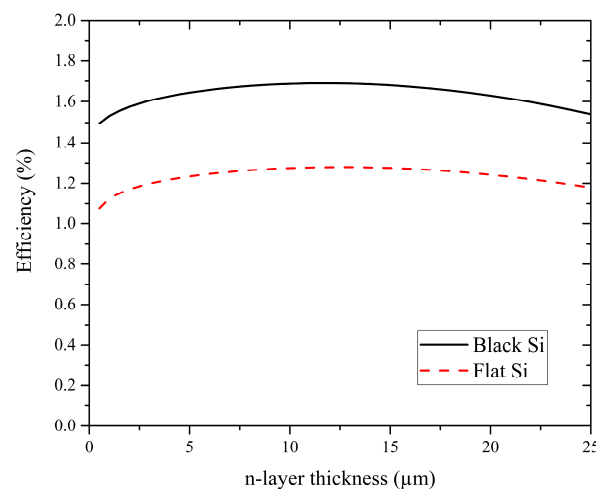


Figure 10. Efficiencies for b-Si cell and flat Si cell at different n-layer thicknesses.

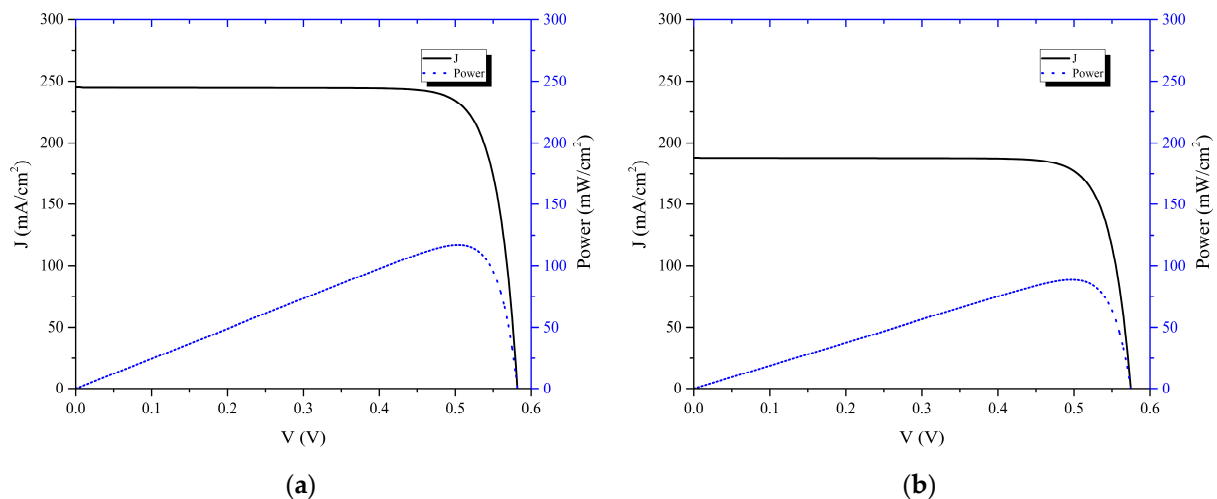


Figure 11. J-V curve for the (a) b-Si and (b) flat Si TPV cell.

3.3. Impact of Heat Generation on Electrical Performance

The impacts of heat generation were shown by comparing the current–voltage characteristics of the simulated black silicon photovoltaic cell. For the comparison below, the b-Si cell with the device parameters in Table 4 was simulated with and without heat generation effects, and the electrical performances were compared. The n- and p-dopant layer thicknesses used were $5.6 \mu\text{m}$ and $45 \mu\text{m}$, respectively. In addition, the dopant concentration in the p-layer was lowered to 10^{15} cm^{-3} to avoid stability issues during the simulation. Similarly, the source spectrum was from a Yb_2O_3 thermal emitter at 1735 K.

The J-V curve obtained for both cases is compared. Figure 12 shows the J-V curves for both cases. From the comparison, it is observed that the short-circuit currents for both cases were similar, but the open circuit voltages decreased when the temperature of the cell increased. This is because the electrons in the lattice have more energy as the cell temperature increases, and hence it requires less energy for the electrons to jump to the conduction band edge. As the energy required to jump between the conduction band edge and the valence band edge decreases, it is analogous to having a lower band gap; hence, the electrical potential achievable by the device also decreases. The difference, albeit small, shows that heat generation in the cell affected the performance of the cell negatively. For comparison, a simulated curve with no heat generation at a cell temperature of 309 K is also shown in the figure. It is visually the same as the EBTM curve, showing that the increase in temperature, regardless of the heat generation mechanism, negatively impacts the cell performance.

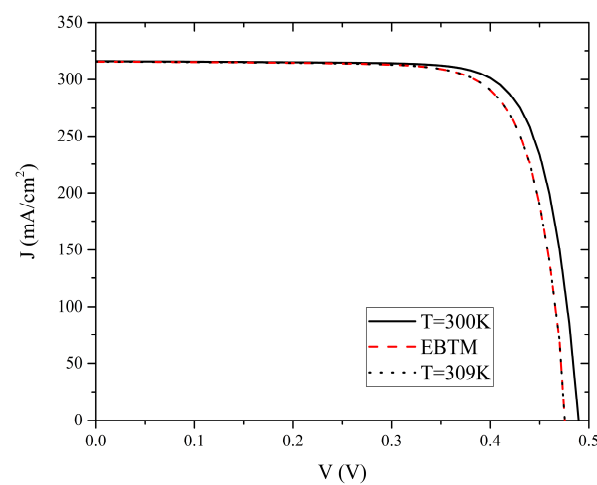


Figure 12. Comparison between the J-V curve for $T = 300$ K, 309 K (no heat generation) and simulation results using the EBTM (with heat generation, $T = 309$ K).

To understand more about the amount of temperature rise in the device, we refer to Figure 13a. The figure shows the temperature of the electrons, optical phonons, and acoustic phonons extracted at the maximum power point of the device. From the figure, the electron and optical phonon temperature rises to a peak of about 550 K in the depletion region in the p-n junction. In the depletion region, the electric field is the highest in the device; hence, it contributes to an exceptional amount of Joule heating to the device. The other term contributing to electron heating is the thermalization of electrons. It is noted that it is assumed that the electrons hold the thermalized energy before the heat energy is relaxed to the optical and acoustic phonons in the equations. Figure 13b shows the amount of heat generation from Joule heating and the thermalization of electrons across the device. The amount of heat generation due to electron thermalization is fairly constant across the device. This contributes to even heating throughout the device. On the other hand, the amount of heat generation due to Joule heating is concentrated in the depletion region, as explained. In this region, the heat generation is about 10 times the amount of thermalized heat and hence contributes to a sharp temperature rise in the depletion region. In addition, due to the low thermal conductivity of the electrons, the energy is not dissipated quickly throughout the device, contributing to the sharp rise in electron and optical phonon temperature.

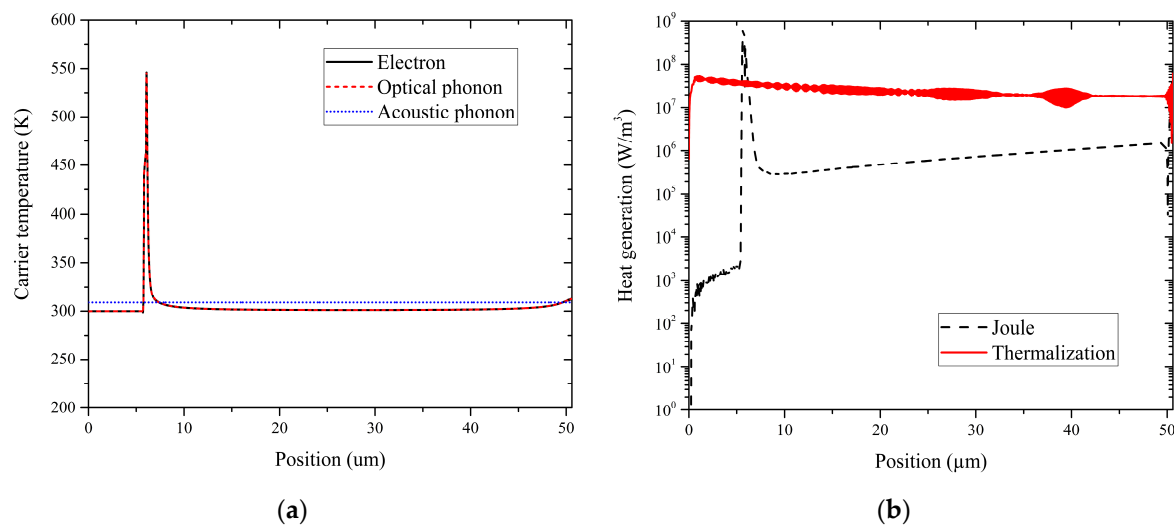


Figure 13. (a) Temperature of different carriers across the b-Si TPV cell, and (b) the heat generation across the device due to Joule heating and electron thermalization.

It is noted that the temperature rise in the cell (9 K) may not be significant in the b-Si cell compared to the temperature of the thermal emitter, which is at 1735 K. This is because the effects of heat conduction and convection from the thermal emitter to the b-Si cell have not been included in the research. However, in real cases, the TPV systems either have vacuum gaps in between the thermal emitter, which minimize heat conduction, or the photovoltaic cell is usually equipped with a cooling system to maintain the temperature of the photovoltaic cell at low temperatures. Hence, the results obtained here may be used as a preliminary guideline for locating hot spots with high heat generation and the predominant mechanism for heat generation in b-Si-based TPV devices.

4. Conclusions

In summary, an opto-electro-thermal simulation model for b-Si photovoltaic cells has been developed. The simulation model was used to simulate the performance of b-Si photovoltaic cells in TPV applications, and the impacts of heat on electrical performance have also been discussed. Results showed that the b-Si layer is useful in increasing the electrical performance of a silicon TPV cell. Heat generation from Joule heating and electron thermalization contributed to some heat generation in TPV cells, which ultimately decreased the performance of the cells. Hence, future studies may focus on studying the application of b-Si surfaces in real silicon TPV systems. Mitigation of heat generation may also be important, and these simulation results can suggest the location and magnitude of heat generation from different mechanisms. The simulation program may be useful in preliminary studies on designing b-Si-based photovoltaic cells in various applications.

Author Contributions: Conceptualization, J.Y.-H.C. and B.T.W.; methodology, J.Y.-H.C.; software, J.Y.-H.C.; validation, J.Y.-H.C.; formal analysis, J.Y.-H.C.; investigation, J.Y.-H.C.; resources, J.Y.-H.C.; data curation, J.Y.-H.C.; writing—original draft preparation, J.Y.-H.C.; writing—review and editing, J.Y.-H.C., B.T.W. and J.S.; visualization, J.Y.-H.C.; supervision, B.T.W.; project administration, J.Y.-H.C. and B.T.W.; funding acquisition, B.T.W. All authors have read and agreed to the published version of the manuscript.

Funding: This research was funded by Ministry of Higher Education, Malaysia, grant number FRGS/1/2018/TK07/SWIN/02/1.

Institutional Review Board Statement: Not applicable.

Informed Consent Statement: Not applicable.

Data Availability Statement: All available data have been reported in this article either in the form of numbers or figures. If additional data are required, the reader may contact the authors.

Acknowledgments: Jasman Y.-H. Chai would like to thank Swinburne University of Technology Sarawak Campus, Malaysia for the partial support of his PhD scholarship.

Conflicts of Interest: The authors declare no conflict of interest.

References

- Chai, J.Y.H.; Wong, B.T.; Juodkakis, S. Black-silicon-assisted photovoltaic cells for better conversion efficiencies: A review on recent research and development efforts. *Mater. Today Energy* **2020**, *18*, 100539. [CrossRef]
- Elsayed, A.A.; Sabry, Y.; Marty, F.; Bourouina, T.; Khalil, D. Optical modeling of black silicon using an effective medium/multi-layer approach. *Opt. Express* **2018**, *26*, 13443. [CrossRef] [PubMed]
- Jürgen Bett, A.; Eisenlohr, J.; Höhn, O.; Repo, P.; Savin, H.; Bläsi, B.; Goldschmidt, J.C. Wave optical simulation of the light trapping properties of black silicon surface textures. *Opt. Express* **2016**, *24*, A434–A445. [CrossRef]
- Kroll, M.; Otto, M.; Käsebier, T.; Füchsel, K.; Wehrspohn, R.; Kley, E.-B.; Tünnermann, A.; Pertsch, T. Black silicon for solar cell applications. In *Photonics for Solar Energy Systems IV*; SPIE: Bellingham, WA, USA, 2012; Volume 8438, pp. 248–258. [CrossRef]
- Lin, C.; Povinelli, M.L. Optical absorption enhancement in silicon nanowire arrays with a large lattice constant for photovoltaic applications. *Opt. Express* **2009**, *17*, 19371–19381. [CrossRef] [PubMed]
- Ma, S.; Liu, S.; Xu, Q.; Xu, J.; Lu, R.; Liu, Y.; Zhong, Z. A theoretical study on the optical properties of black silicon. *AIP Adv.* **2018**, *8*, 035010. [CrossRef]
- Nguyen, K.; Abi-Saab, D.; Basset, P.; Richalot, E.; Malak, M.; Pavy, N.; Flourens, F.; Marty, F.; Angelescu, D.; Leprince-Wang, Y.; et al. Study of black silicon obtained by cryogenic plasma etching: Approach to achieve the hot spot of a thermoelectric energy harvester. *Microsyst. Technol.* **2012**, *18*, 1807–1814. [CrossRef]
- Nguyen, K.N.; Abi-Saab, D.; Malak, M.; Basset, P.; Richalot, E.; Pavy, N.; Flourens, F.; Marty, F.; Angelescu, D.; Leprince-Wang, Y.; et al. Study of black silicon obtained by deep reactive ion etching—Approach to achieving the hot spot of a thermoelectric energy harvester. In *Proceedings of the DTIP 2011—Symposium on Design, Test, Integration and Packaging of MEMS/MOEMS*, Aix-en-Provence, France, 11–13 May 2011.
- Patchett, S.; Khorasaninejad, M.; Nixon, O.; Saini, S. Effective index approximation for ordered silicon nanowire arrays. *J. Opt. Soc. Am. B* **2013**, *30*, 306. [CrossRef]
- Rahman, T.; Boden, S.A. Optical modeling of black silicon for solar cells using effective index techniques. *IEEE J. Photovolt.* **2017**, *7*, 1556–1562. [CrossRef]
- Rahman, T.; Bonilla, R.S.; Nawabjan, A.; Wilshaw, P.R.; Boden, S.A. Passivation of all-angle black surfaces for silicon solar cells. *Sol. Energy Mater. Sol. Cells* **2017**, *160*, 444–453. [CrossRef]
- Ravindra, N. Modeling of optical properties of black silicon/crystalline silicon. *J. Sci. Ind. Metrol.* **2015**, *1*, 100001. [CrossRef]
- Steglich, M.; Käsebier, T.; Zilk, M.; Pertsch, T.; Kley, E.-B.; Tünnermann, A. The structural and optical properties of black silicon by inductively coupled plasma reactive ion etching. *J. Appl. Phys.* **2014**, *116*, 173503. [CrossRef]
- Tucher, N.; Gebrewold, H.T.; Blasi, B. Field stitching approach for the wave optical modeling of black silicon structures. *Opt. Express* **2018**, *26*, A937–A945. [CrossRef] [PubMed]
- Tyson, J.; Rahman, T.; Boden, S. Optical simulation of black silicon surfaces using geometric randomisation and unit-cell based averaging. In *Proceedings of the 15th Photovoltaic Science, Application and Technology Conference*, Coventry, UK, 10–12 April 2019; pp. 1–4.
- Wang, B.; Leu, P.W. Enhanced absorption in silicon nanocone arrays for photovoltaics. *Nanotechnology* **2012**, *23*, 194003. [CrossRef] [PubMed]
- Chai, J.Y.H.; Wong, B.T.; Juodkakis, S. Comparison between one-dimensional and three-dimensional optical modelling of ordered black silicon nanostructures using effective medium approach. In *Proceedings of the 10th International Conference on Nano and Materials Science 2022*, Singapore, 12–14 February 2022.
- Kane, Y. Numerical solution of initial boundary value problems involving maxwell’s equations in isotropic media. *IEEE Trans. Antennas Propag.* **1966**, *14*, 302–307. [CrossRef]
- Sullivan, D.M. *Electromagnetic Simulation Using the FDTD Method*, 2nd ed.; John Wiley & Sons: Hoboken, NJ, USA, 2013. [CrossRef]
- Rumpf, R. Electromagnetic Analysis Using Finite-Difference Time-Domain. Available online: <https://empossible.net/academics/emp5304/> (accessed on 10 March 2022).
- Green, M.A.; Keevers, M.J. Optical properties of intrinsic silicon at 300 k. *Prog. Photovolt. Res. Appl.* **1995**, *3*, 189–192. [CrossRef]
- Wurfel, P. *Physics of Solar Cells: From Principles to New Concepts*; John Wiley & Sons: Hoboken, NJ, USA, 2005. [CrossRef]
- Entner, R. *Modeling and Simulation of Negative Bias Temperature Instability*; AV Akademikerverlag: Judendorf-Straßengel, Austria, 2012.
- Vasileška, D.; Goodnick, S.M.; Klimeck, G. *Computational Electronics: Semiclassical and Quantum Device Modeling and Simulation*, 1st ed.; CRC Press: Boca Raton, FL, USA, 2010; p. 782.
- Stratton, R. Diffusion of hot and cold electrons in semiconductor barriers. *Phys. Rev.* **1962**, *126*, 2002–2014. [CrossRef]
- Grasser, T.; Ting-Wei, T.; Kosina, H.; Selberherr, S. A review of hydrodynamic and energy-transport models for semiconductor device simulation. *Proc. IEEE* **2003**, *91*, 251–274. [CrossRef]

27. *Atlas User's Manual*; Silvaco Inc.: Santa Clara, CA, USA, 2016.
28. Vasileska, D. Introduction to dd Modeling with Padre. Available online: <https://nanohub.org/resources/1516> (accessed on 16 December 2022).
29. Zhou, J.; Yi, Q.; Wang, Y.; Ye, Z. Temperature distribution of photovoltaic module based on finite element simulation. *Sol. Energy* **2015**, *111*, 97–103. [[CrossRef](#)]
30. Bitnar, B.; Durisch, W.; Holzner, R. Thermophotovoltaics on the move to applications. *Appl. Energy* **2013**, *105*, 430–438. [[CrossRef](#)]
31. Bitnar, B.; Durisch, W.; Mayor, J.C.; Sigg, H.; Tschudi, H.R. Characterisation of rare earth selective emitters for thermophotovoltaic applications. *Sol. Energy Mater Sol. Cells* **2002**, *73*, 221–234. [[CrossRef](#)]
32. Striemer, C.C.; Fauchet, P.M. Dynamic etching of silicon for broadband antireflection applications. *Appl. Phys. Lett.* **2002**, *81*, 2980–2982. [[CrossRef](#)]

Disclaimer/Publisher's Note: The statements, opinions and data contained in all publications are solely those of the individual author(s) and contributor(s) and not of MDPI and/or the editor(s). MDPI and/or the editor(s) disclaim responsibility for any injury to people or property resulting from any ideas, methods, instructions or products referred to in the content.